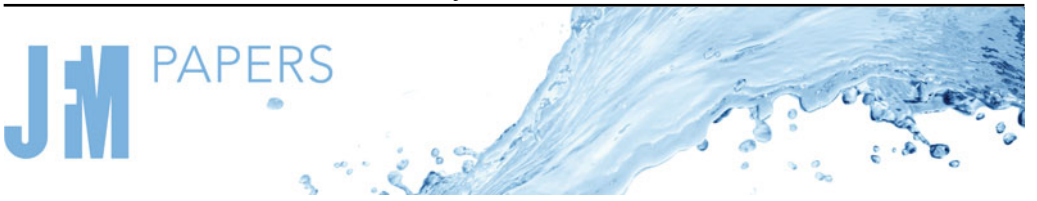
J. Fluid Mech. (2026), *vol.* 1041, A3, doi:10.1017/jfm.2026.11903



An inverse-square force between evaporating sessile droplets

Zhi Wu Jiang[1], **Zuo Han Wen**[1], **Hang Ding**[1] and **Er Qiang Li**[1]

[1]State Key Laboratory of High Temperature Gas Dynamics, School of Engineering Science, University of Science and Technology of China, Hefei 230027, PR China

Corresponding author: Er Qiang Li, eqli@ustc.edu.cn

(Received 22 October 2025 UTC; revised 23 April 2026 UTC; accepted 30 June 2026 UTC)

In this study, we present the discovery of an inverse-square force between evaporating sessile droplets. We find that one evaporating sessile droplet exerts a driving force on another, with the magnitude of the force decaying inversely proportional to the square of distance between their centres. The inverse-distance decay of the vapour concentration generated by the source droplet is a key ingredient leading to the inverse-square form of the force. A theoretical framework combining continuum hydrodynamics with an effective capillary line-force representation is developed to rationalize this force. The inverse-square form is robust over ranges of droplet size, composition and ambient humidity. Its broader applicability is further supported by our analysis of previously published kinematic data for pure-liquid sessile droplets and thermocapillary floating droplets.

Key words: drops, contact lines, condensation/evaporation

1. Introduction

Evaporating sessile droplets are ubiquitous in natural and technological processes, including inkjet printing and biological systems, among others, and play a crucial role in a wide range of interfacial phenomena (Deegan *et al.* 1997; Lohse & Zhang 2020; Masoud *et al.* 2021; Wilson & D'Ambrosio 2023). When multiple droplets evaporate in proximity, the vapour fields overlap, leading to spatially heterogeneous vapour concentration distributions around neighbouring droplets, which generate local surface tension gradients. Such gradients can induce droplet motion and collective dynamics, yet a quantitative description linking experimentally observed trajectories to the underlying driving mechanisms remains an open challenge.

https://doi.org/10.1017/jfm.2026.11903 Published online by Cambridge University Press

© The Author(s), 2026. Published by Cambridge University Press.

A central mechanism underlying vapour-mediated droplet motion is the emergence of surface tension gradients along the droplet interface. In binary or miscible droplets, local variations in vapour concentration modify the interfacial composition distribution through vapour–liquid equilibrium, generating Marangoni stresses that propel the droplet (Cira *et al.* 2015; Malinowski *et al.* 2020). Conversely, for two adjacent droplets of different pure liquids, directional motion can arise from vapour adsorption onto a thin precursor film or the liquid–vapour interface of bulk liquid, inducing local surface tension variations (Bangham & Saweris 1938; Man & Doi 2017). In both cases, the net driving force can be effectively described by the spatial gradient of a scalar field – vapour concentration or temperature – coupled to surface stress along the interface.

Bangham & Saweris (1938) first observed that vapour-mediated interactions can be either attractive or repulsive. A droplet with lower surface tension is drawn towards the vapour of a higher-surface-tension droplet, while a droplet with higher surface tension is repelled. These interactions depend on relative composition or local humidity gradients. Subsequent studies extended these ideas to droplets on substrates or in capillary channels, considering both pure liquids and binary mixtures (Cira *et al.* 2015; Sadafi *et al.* 2019). Building on this foundation, Zhao *et al.* (2025) proposed a theoretical model combining vapour adsorption and evaporation effects, successfully predicting conditions for motion reversal in binary droplets and providing a unified description of pure and binary systems. While previous models capture the general effects of vapour gradients on droplet motion, they rarely establish a direct, experimentally accessible connection between theory and observed droplet trajectories, motivating the present study.

In addition to vapour-mediated surface tension gradients driving droplet motion, the apparent contact angle is also sensitive to local humidity. In multicomponent evaporating droplets, preferential evaporation near the contact line generates surface tension gradients, inducing inward Marangoni flows and promoting droplet contraction. This effect has been analysed using lubrication theory and numerical simulations, revealing power-law dependencies of the apparent contact angle on relative humidity (Diddens 2017; Diddens *et al.* 2017*a*,*b*; Karpitschka *et al.* 2017; Williams *et al.* 2021; Wu *et al.* 2021; Gelderblom *et al.* 2022), which provide a quantitative link between microscopic dynamics and measurable droplet shapes. For instance, Cira *et al.* (2015) heuristically reported a linear dependence of $\cos\theta$ on ϕ, whereas Karpitschka *et al.* (2017) derived $\theta \sim (\phi_{eq} - \phi)^{1/3}$ using a lubrication-theory approach. The more recent model (Wu *et al.* 2021) incorporating Marangoni contraction predicts $\theta \sim (\phi_{eq} - \phi)^{1/2}$, in qualitative agreement with experimental results from Cira *et al.* (2015). Furthermore, vapour-driven solutal Marangoni flows have been shown to undergo directional transitions when the local vapour concentration crosses the vapour–liquid equilibrium associated with droplet composition, emphasizing the role of local thermodynamic imbalances at the contact line (Ryu *et al.* 2025).

These studies highlight the intricate coupling between evaporation, composition, surface tension and hydrodynamic flow near the contact line, showing that droplet motion is influenced by both quasistatic thermodynamic effects and dynamically sustained Marangoni stresses at the microscopic scale. Consequently, observed dependencies of the apparent contact angle on humidity can often be interpreted consistently from either a quasiequilibrium perspective or a dynamical Marangoni-flow framework. This intrinsic coupling motivates the use of effective or calibrated relations between vapour conditions and interfacial stresses, allowing a practical modelling framework without specifying the dominant microscopic mechanism.

https://doi.org/10.1017/jfm.2026.11903 Published online by Cambridge University Press

	Density ρ (kg m^{-3})	Surface Tension γ (mN m^{-1})	Dynamic Viscosity μ (mPas)
Air	1.20	—	0.018
Water	998	72.7	1.0
PG	1038	35.7	56.0
10 wt% PG aqueous solution	1005	59.2	1.4
20 wt% PG aqueous solution	1014	55.7	2.0
40 wt% PG aqueous solution	1032	47.8	4.6
60 wt% PG aqueous solution	1043	38.7	9.4

Table 1. Properties of the liquids used in the experiments. All values were measured at 20°C.

In the present study, we investigate pairs of propylene glycol (PG)–water sessile droplets, i.e. droplets resting on solid substrates, in which solutal Marangoni stresses dominate under ambient conditions. Under quasistatic dynamics, the relative motion of droplet pairs can be represented by a simple cubic relation between the distance and time, $d^3 - (R_1 + R_2)^3 \propto t$, where $d = L + R_1 + R_2$ is the centre-to-centre distance, L the edge-to-edge separation, R_1 and R_2 the mean spreading radii of a pair. Compared with previous work, the present study extends the understanding of vapour-mediated droplet interactions in several distinct aspects. First, by establishing an effective calibration between local vapour conditions and contact-line response, we provide an experimentally accessible link between humidity gradients and the inverse-square force that governs droplet motion. Then, we examine the robustness of the inverse-square law between droplets of identical or unequal size and composition by showing that the corresponding cubic kinematic relation consistently captures the relative motion across all cases. Finally, we compare our results with published data for single-component droplets and floating droplets driven by thermocapillary effects, indicating that the inverse-square force scaling may represent a general feature of droplet interactions mediated by scalar-field gradients. These findings provide a practical and experimentally accessible framework for analysing evaporating droplet interactions at the level of droplet pairs, and establish a quantitative basis for linking droplet kinematics to the underlying physical mechanisms.

2. Experimental methodology

The PG ($\geqslant$99.5 %) was obtained from Sigma–Aldrich. Deionized water (resistivity $>$18.2 MΩ cm) was produced from a Milli-Q purification system. Single-side-polished, p-type silicon wafers with a thickness of 1 mm were purchased from UniversityWafer, Inc. Aqueous PG solutions were prepared to give the desired mass fractions, and the relevant physical properties of the liquids used in the experiments are summarized in table 1.

In the experiments, two droplets made of the same PG aqueous solution were gently deposited onto a pristine, oxygen-plasma-cleaned silicon wafer. All droplets were freshly prepared immediately before deposition to ensure uniform composition, and were deposited before any noticeable evaporation occurred. Their interactions were recorded with a high-resolution digital camera (8K RED DSMC2, RED Digital Cinema, LLC.). To control the ambient humidity and temperature, experiments were carried out in an environmental chamber (5503-1-11-100-1741, Electro-Tech Systems, Inc.). The droplet configuration is shown in figure 1, and a sketch of the experimental set-up is shown in figure 2(*b*). The tested parameters include droplet volumes Ω ranging from 0.07 to 0.80 µL and ambient relative humidity ϕ_∞ ranging from 19.9 % to 81.1 %.

https://doi.org/10.1017/jfm.2026.11903 Published online by Cambridge University Press

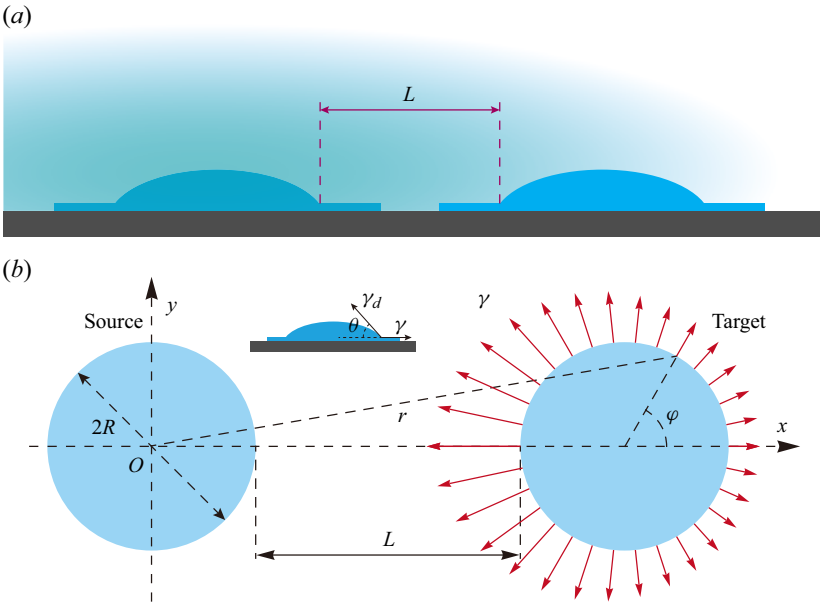


Figure 1. Attraction between two binary droplets. (*a*) Schematic illustration introducing the 'source' and 'target' droplets used for analysis. The target droplet is exposed to a non-uniform vapour concentration field generated by a neighbouring 'source' droplet. For clarity, only the vapour field produced by the 'source' droplet is shown. The source-facing side of the target droplet is subject to a higher local vapour concentration than the opposite side, providing the physical basis for the vapour-mediated interaction. (*b*) Schematic showing the change in surface tension γ along the periphery of the 'target' drop, arising from local vapour–liquid equilibrium within the precursor film. The inset: γ_d the surface tension of the bulk droplet liquid; γ the surface tension in the precursor liquid film; θ the contact angle.

3. Results and discussion

3.1. *Droplet movement*

When a droplet consisting of miscible liquids is located on a superhydrophilic substrate, it has been shown that the interplay among Marangoni flow, capillary flow, diffusive transport and evaporation will lead to a droplet profile with an apparent non-zero contact angle, even though each of the liquid components fully wets the substrate (Cira *et al.* 2015; Karpitschka *et al.* 2017; Lohse & Zhang 2020; Hack *et al.* 2021). This phenomenon is also observed in our experiments for 10 wt % PG droplets.

A representative experiment is illustrated in figure 2(*a*) (corresponding to Supplementary movie 1), where two identical 10 wt % PG droplets, initially separated by an edge-to-edge distance L, gradually migrate towards each other and eventually coalesce. The radius is $R = 1.55$ mm and the ambient relative humidity ϕ_∞ is 56.9 %. Figure 2(*c*) shows the repeatability of the experiment. During the experiments, the droplets have a mean spreading radius $R = 1.37$ mm, and the surrounding relative humidity is $\phi_\infty = 51.3$ %. This case was repeated at least 10 times, and error bars represent standard deviations across repetitions.

3.2. *Droplet pair interaction*

To rationalize the experimentally observed dynamics, we revisit the fundamental governing equations and boundary conditions governing the coupled vapour–liquid

https://doi.org/10.1017/jfm.2026.11903 Published online by Cambridge University Press

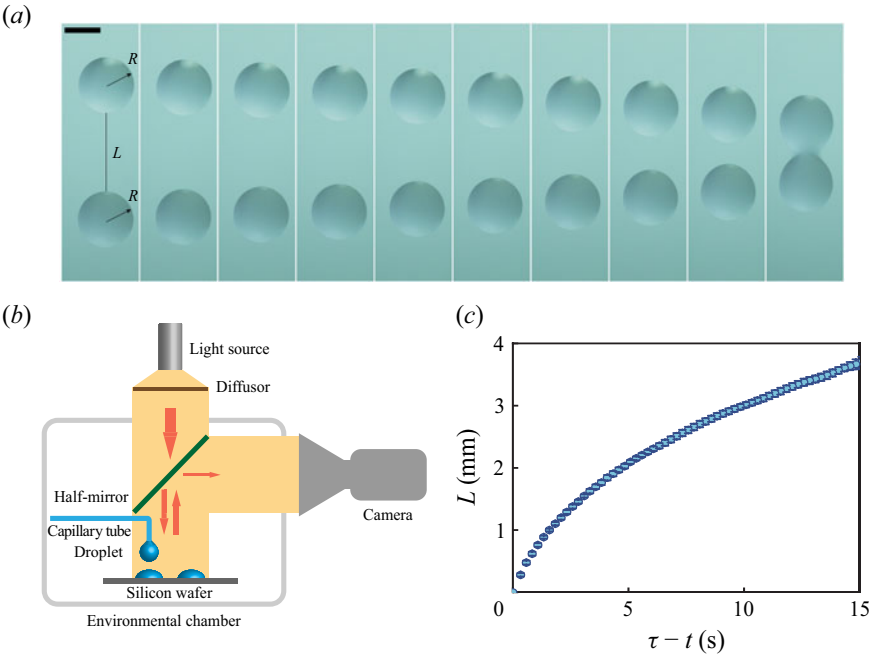


Figure 2. Attraction between two binary droplets. (*a*) Top view (Supplementary movie 1) showing attraction of two 10 wt % PG sessile droplets of the same size on a hydrophilic silicon substrate, for $R = 1.55$ mm, $\phi_\infty = 56.9\,\%$ and room temperature of 20 °C. Sequence of images spaced by 1.67 s. Scale bar is 2 mm. (*b*) Sketch of the experimental configuration, showing the capillary microtube used to pinch off the droplet. (*c*) Mean distance between droplets as a function of time before contact for two moving 10 wt % PG droplets. Here $R = 1.37 \pm 0.02$ mm and $\phi_\infty = 51.3\,\% \pm 2.0\,\%$. The error bars represent the standard deviation of 10 experiments.

system. Our objective is to derive a quantitative description of the droplet evolution directly from the governing equations of continuum hydrodynamics. To render the problem analytically tractable while retaining the essential physics, we adopt the following assumptions. (i) The source droplet is treated as an isolated evaporating droplet, and the influence of the target droplet on the evaporation of the source droplet is neglected. The vapour concentration field in the surrounding gas phase is quasisteady and diffusion-dominated, and therefore satisfies Laplace's equation. (ii) Vapour-induced variations in surface tension are localized near the contact line, where a nanometric precursor film exists. These variations give rise to an effective driving force acting at the contact line, while the surface tension of the droplet bulk remains uniform. (iii) The flow inside each droplet is quasistatic and inertia-free, and is governed by the Stokes equations. This modelling framework follows that introduced by Cira *et al.* (2015). The schematic illustration is shown in figure 1.

Then, we estimate the relevant dimensionless numbers characterizing the droplet dynamics. Unless otherwise specified, the characteristic droplet radius is taken as $R = 1$ mm, consistent with the experimental range $R \in [0.8, 1.8]$ mm. The characteristic migration velocity is estimated from the measured trajectories as $U \sim 10^{-4}\,\mathrm{m\,s^{-1}}$. All material properties are taken from table 1 and correspond to $T = 293$ K and $p = 1$ atm. The Reynolds number, $Re = \rho U R/\mu$ is estimated to be $Re \sim O(10^{-2}) \ll 1$ for all PG aqueous solutions considered. This indicates that inertial effects are negligible, and

https://doi.org/10.1017/jfm.2026.11903 Published online by Cambridge University Press

the internal flow within the droplets can be well described by the Stokes equations. The capillary number, $Ca = \mu U/\gamma$ is found to be $O(10^{-6})$ across the experimental parameter space. This indicates that viscous stresses are far too weak to induce appreciable deformation of the liquid–air interface. Accordingly, the droplet shape may be regarded as quasistatic and governed by instantaneous capillary equilibrium. The relative importance of gravity is quantified by the Bond number $Bo = \rho g R^2/\gamma$, which remains $Bo \sim 0.1$ for the droplets studied here. This implies that gravitational effects are secondary compared with surface tension at the droplet scale considered.

Taken together, these estimates delineate a consistent asymptotic regime in which interfacial dynamics are governed by capillarity, while inertial effects are negligible compared with viscous dissipation. This provides the basis for the droplet dynamics model developed below.

3.2.1. *Governing equations and force–velocity relation*

We develop a theoretical framework to relate the translational motion of an evaporating sessile droplet to the balance of capillary force arising under vapour-mediated interactions and viscous drag force. The analysis is restricted to the quasistatic regime relevant to the present experiments, in which inertial effects are negligible and the droplet shape adjusts rapidly compared with the time scale of translation. Under these conditions, the flow inside the droplet is governed by incompressible Stokes equations. The velocity field $\boldsymbol{u}(\boldsymbol{x})$ and pressure $p(\boldsymbol{x})$ satisfy $\boldsymbol{\nabla}\cdot\boldsymbol{\sigma} = \boldsymbol{0}$ and $\boldsymbol{\nabla}\cdot\boldsymbol{u} = 0$, where the Newtonian stress tensor is given by $\boldsymbol{\sigma} = -p\boldsymbol{I} + \mu[\boldsymbol{\nabla u} + (\boldsymbol{\nabla u})^T]$.

The liquid–solid interface is modelled using a Navier-slip boundary condition, $\boldsymbol{u}_s = l_s\boldsymbol{\tau}_s/\mu$ where l_s is the slip length and $\boldsymbol{\tau}_s$ is the tangential stress at the liquid–solid interface S_{ls}. On the liquid–air interface S_{lg}, the normal stress is balanced by capillarity $\boldsymbol{\sigma}\cdot\boldsymbol{n} = \gamma_d\kappa\boldsymbol{n}$, where $\boldsymbol{n}$ is the outward unit normal, γ_d is the surface tension of the bulk droplet and κ is the mean curvature. Numerical simulations of evaporating binary droplets show that surface tension gradients are strongly localized within a narrow region near the contact line (Karpitschka *et al.* 2017; Diddens *et al.* 2017*a*; Dekker *et al.* 2026). In this region, the surface tension gradient follows a power law dependence on the distance s to the contact line, scaling as $\sim s^{-3/2}$ (Ramírez-Soto & Karpitschka 2022). Following previous analyses of vapour-mediated droplet interactions, the system is described using a simplified picture of a droplet consisting of a bulk phase with a single, spatially uniform composition, surrounded by a nanometric precursor film whose composition may vary along the substrate. Within the precursor film, local phase equilibrium at the liquid–air interface constrains the liquid composition to adjust to the vapour partial pressure above the surface. Spatial variations in vapour concentration therefore alter the local vapour partial pressure, which shifts the equilibrium liquid composition and hence the surface tension within the film (Wang *et al.* 2021; Chao *et al.* 2022; Zhao *et al.* 2025). Because the surface stresses are confined to a region small compared with the droplet size, their integrated effect at macroscopic scales can be effectively represented by a line force acting at the apparent contact line, consistent with Cira *et al.* (2015) and Zhao *et al.* (2025). When this effective line force becomes azimuthally unbalanced, a net driving force arises and the droplet undergoes motion.

To relate the translational velocity of the droplet to this net force, we employ the Lorentz reciprocal theorem for incompressible Stokes flows (Happel & Brenner 2012; Masoud & Stone 2014, 2019). We define an auxiliary flow $(\hat{\boldsymbol{u}}, \hat{\boldsymbol{\sigma}})$ in the same instantaneous droplet geometry, corresponding to the rigid-body translation of the droplet with prescribed

https://doi.org/10.1017/jfm.2026.11903 Published online by Cambridge University Press

velocity $\hat{\boldsymbol{U}}$ along the substrate, sharing the same direction with the actual droplet motion. The boundary conditions are chosen to satisfy the following principles: on the liquid–solid interface S_{ls}, the auxiliary flow obeys the same Navier-slip condition as the actual flow, namely $\hat{\boldsymbol{u}}_s = l_s \hat{\boldsymbol{\tau}}_s/\mu$, to ensure that stress integrals at the contact line converge; on the liquid–air interface S_{lg}, the auxiliary velocity is prescribed as a rigid-body translation, $\hat{\boldsymbol{u}} = \hat{\boldsymbol{U}}$, thereby isolating the translational degree of freedom in the Lorentz reciprocal theorem analysis; finally, the auxiliary flow vanishes in the far field, $\hat{\boldsymbol{u}} \to 0$ as $r \to \infty$, so that the surface integrals form a closed system.

In the auxiliary problem, the surface tension is uniform and the interface shape is held fixed. This choice is justified by the quasistatic nature of the dynamics, for which shape relaxation occurs on time scales much shorter than translational motion. The auxiliary problem therefore isolates the translational degree of freedom while preserving the hydrodynamic boundary conditions.

The Lorentz reciprocal theorem states that

$$\int_S \hat{\boldsymbol{u}} \cdot (\boldsymbol{\sigma} \cdot \boldsymbol{n}) \, \mathrm{d}S = \int_S \boldsymbol{u} \cdot \left(\hat{\boldsymbol{\sigma}} \cdot \boldsymbol{n}\right) \, \mathrm{d}S, \tag{3.1}$$

where $S = S_{lg} \cup S_{ls}$ is a closed surface enclosing the fluid domain. On the liquid–air interface S_{lg}, $\int_{S_{lg}} \boldsymbol{u} \cdot (\hat{\boldsymbol{\sigma}} \cdot \boldsymbol{n}) \, \mathrm{d}S = \boldsymbol{U} \cdot \int_{S_{lg}} (\hat{\boldsymbol{\sigma}} \cdot \boldsymbol{n}) \, \mathrm{d}S$, where $\boldsymbol{U}$ represents the translational velocity of the droplet's centre of mass. On the liquid–solid interface S_{ls}, both $\boldsymbol{u}$ and $\hat{\boldsymbol{u}}$ satisfy the same Navier-slip condition, so contributions to the surface integrals are balanced, $\int_{S_{ls}} \boldsymbol{u} \cdot \hat{\tau}_s \mathrm{d}S = \int_{S_{ls}} \boldsymbol{u} \cdot (\mu \hat{\boldsymbol{u}}/l_s) \mathrm{d}S = \int_{S_{ls}} \hat{\boldsymbol{u}} \cdot \tau_s \mathrm{d}S$.

The integral reduces to

$$\hat{\boldsymbol{U}} \cdot \boldsymbol{F} = \boldsymbol{U} \cdot \hat{\boldsymbol{F}}_d, \tag{3.2}$$

where $\boldsymbol{F} = \int_{S_{lg}} (\boldsymbol{\sigma} \cdot \boldsymbol{n}) \mathrm{d}S = \int_C \gamma \boldsymbol{t} \, \mathrm{d}l$ is the net capillary driving force concentrated along the contact line, $\boldsymbol{t}$ being the unit vector tangent to the substrate.

Under the small contact angle condition, the velocity of the auxiliary flow can be described by lubrication function (Snoeijer & Andreotti 2013),

$$\nabla \cdot \left(h^3 \nabla \hat{p}\right) = 6\mu \hat{\boldsymbol{U}} \cdot \nabla h. \tag{3.3}$$

The total hydrodynamic resistance $\hat{\boldsymbol{F}}_d$ in the auxiliary field is dominated by logarithmic singularity of the wetting perimeter. This yields the characteristic scaling, $\hat{F}_d = \xi \mu R \hat{U} l_n/\theta$. Equation (3.2) provides a rigorous connection between droplet velocity and capillary forcing, independent of the detailed internal flow structure, yields

$$\frac{\xi R \mu l_n}{\theta} \boldsymbol{U} = \int_C \gamma \boldsymbol{t} \, \mathrm{d}l, \tag{3.4}$$

where l_n denotes the logarithmic cutoff factor arising from the viscous stress singularity near the contact line, and ξ is a dimensionless coefficient of order unity reflecting details of the microscopic flow structure. Equation (3.4) can be rewritten as $F_d = F$, where the functional form of drag force reads $F_d = \xi \mu R U l_n/\theta$. The droplet velocity is determined once the effective surface tension in the contact-line region is related to the ambient vapour distribution, which is addressed in the following sections.

https://doi.org/10.1017/jfm.2026.11903 Published online by Cambridge University Press

3.2.2. *Humidity distribution around sessile droplets*

When analysing the motion of a target droplet, we take the vapour concentration field imposed by a neighbouring 'source' droplet as the relevant driving field. Evaporation of a sessile droplet under ambient conditions is governed by diffusion in the surrounding gas phase (Picknett & Bexon 1977; Deegan *et al.* 1997, 2000; Hu & Larson 2002), so the local vapour concentration ϕ satisfies

$$\frac{\partial \phi}{\partial t} = D_v \nabla^2 \phi, \tag{3.5}$$

where D_v is the diffusion coefficient of water vapour in air. In the present water–PG system, evaporation is dominated by water because the saturation vapour pressure of water ($p_{sat}^{H_2O} \approx 2.3\,\text{kPa}$) is orders of magnitude larger than that of PG ($p_{sat}^{PG} \approx 10\,\text{Pa}$) under ambient conditions (Stull 2002; Wagner & Pruß 2002). Although vapour-phase PG adsorption can affect droplet motion in sufficiently dilute PG solutions (Zhao *et al.* 2025), the concentrations considered here lie outside that regime (figure S6 in the Supplementary material). We therefore neglect PG vapour adsorption and treat the vapour phase as a water–air mixture, with PG taken as effectively non-volatile. For simplicity, we express the vapour field in terms of the relative humidity $\phi(r)$, where r is the distance from the centre of the 'source' droplet. The relevant vapour Péclet number is $Pe_v = UR/D_v$. Using $D_v = 2.6 \times 10^{-5}\,\text{m}^2\,\text{s}^{-1}$ at $T = 293\,\text{K}$ and $p = 1\,\text{atm}$ (Hu & Larson 2002), we obtain $Pe_v \sim O(10^{-3})$, indicating diffusion-dominated and quasisteady transport. The humidity field therefore satisfies

$$\nabla^2 \phi = 0, \tag{3.6}$$

which forms the basis of the vapour-field analysis in this study.

The droplets in the experiments are sessile spherical caps of contact angle θ on a solid substrate. Since the vapour field around an evaporating sessile droplet depends on geometric confinement (Benusiglio *et al.* 2017), the chamber dimensions are chosen to be at least two orders of magnitude larger than the droplet size, and the droplets are placed sufficiently far from the walls so that confinement effects are negligible. Following the treatment by Cira *et al.*, the droplets considered here are predominantly composed of water (10 wt % PG by volume, corresponding to 2.6 % PG in mole fraction), and the water vapour at the liquid–air interface is therefore assumed to be locally saturated (Raoult 1887; Saxena & Hildemann 1997; Cira *et al.* 2015; Zhao *et al.* 2025). A no-flux condition is imposed on the dry substrate outside the droplet footprint, and the ambient humidity ϕ_∞ is recovered in the far field. Under these boundary conditions, Laplace's equation admits an analytical solution, derived in toroidal coordinates (Picknett & Bexon 1977; Hu & Larson 2002),

$$\frac{\phi - \phi_\infty}{1 - \phi_\infty} = \sqrt{2\cosh\alpha - 2\cos\beta} \times \int_0^\infty \frac{\cosh(\theta\omega)}{\cosh(\pi\omega)} \frac{\cosh[(2\pi - \beta)\omega]}{\cosh[(\pi - \theta)\omega]} P_{-1/2+i\pi}(\cosh\alpha)\,\mathrm{d}\omega, \tag{3.7}$$

where α and β are toroidal coordinates related to the cylindrical coordinates (r, z), and $P_{-1/2+i\pi}(\cosh\alpha)$ denotes the Legendre function of the first kind.

Of particular relevance for droplet–droplet interactions is the vapour concentration distribution along the substrate outside the droplet footprint. Since the vapour concentration converges within the small experimental contact angles ranging $5^\circ \leqslant \theta \leqslant 15^\circ$, the analytical solution can be reasonably simplified and reduced to

https://doi.org/10.1017/jfm.2026.11903 Published online by Cambridge University Press

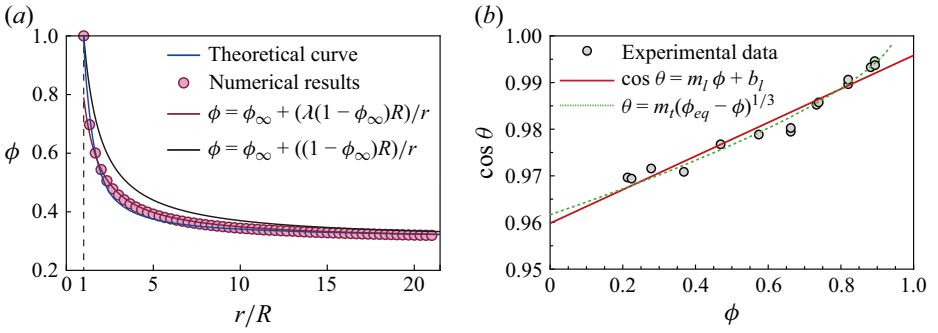


Figure 3. (*a*) The local relative humidity ϕ along the substrate. Blue curve, theoretical results (3.8), for a thin film with $\theta = 0$; dots, numerically solved results of ϕ, for the ambient humidity in the far field $\phi_\infty = 30.0\,\%$ and $\theta = 10°$; red curve, $\phi(r) = \lambda(1-\phi_\infty)R/r + \phi_\infty$, an asymptotic solution of (3.8) with $\lambda = 0.735$; black curve, centrosymmetric solution of $\phi(r)$ for the evaporation from a drop floating freely in the air (Cira *et al.* 2015). (*b*) Apparent contact angle θ as a function of ambient relative humidity ϕ for a 10 wt % PG droplet on a hydrophilic silicon substrate. The fitting coefficients are $m_l = 0.036$ and $b_l = 0.96$, $m_t = 0.28$ and $\phi_{eq} = 0.95$, for two models, respectively.

the classical problem of diffusion from a circular disk into a half-space. Along the substrate ($z = 0$), the vapour concentration exhibits an inverse-distance dependence on the horizontal distance r,

$$\frac{\phi - \phi_\infty}{1-\phi_\infty} = \frac{1}{2} - \frac{1}{\pi}\arctan\left[\frac{r^2 - 2R^2}{2R\sqrt{r^2-R^2}}\right],\ r > R, \tag{3.8}$$

$$\left.\frac{\partial\phi}{\partial r}\right|_d = -(1-\phi_\infty)\,\frac{2}{\pi d}\,\frac{R}{\sqrt{d^2-R^2}} = -(1-\phi_\infty)\,\frac{\lambda(d)R}{d^2}, \tag{3.9}$$

where $d = L + 2R \in [2R, +\infty)$ is the centre-to-centre distance of two droplets, and $\lambda(d) = 2/(\pi\sqrt{1-R^2/d^2})$. Notably, $\lambda(d)$ is a slowly varying, order-unity function of the separation, bounded between its near-field and far-field limits, $\lambda(2R) = 4/(\sqrt{3}\pi)$, $\lambda(\infty) = 2/\pi$. In the following analysis, we take $\lambda = \lambda(2R) \simeq 0.735$, and the humidity distribution can be expressed as

$$\phi(r) = \phi_\infty + \lambda(1-\phi_\infty)\frac{R}{r}. \tag{3.10}$$

In this representation, geometric effects are fully absorbed into λ, while the humidity field retains a universal functional form (figure 3*a*).

To assess the validity of this asymptotic representation, we performed finite-element simulations of Laplace's equation. The numerical results confirm that, for $\theta \lesssim 30°$, the vapour concentration profiles along the substrate collapse onto a nearly universal curve that is weakly dependent on the contact angle (figure S1 in the Supplementary material), thereby supporting the validity of (3.10) over the experimentally relevant range.

3.2.3. *Dependence of contact angle on humidity*

To quantify the effect of ambient humidity on the effective surface tension at the contact line, we consider a sessile droplet in a spatially uniform environment with prescribed relative humidity ϕ. In this setting, the droplet remains stationary and the humidity field is homogeneous, the variations in the surface tension are reflected in changes in the apparent contact angle θ, as given by the horizontal force balance at the intersection of the thin

https://doi.org/10.1017/jfm.2026.11903 Published online by Cambridge University Press

film and the bulk droplet, $\gamma = \gamma_d \cos\theta$. The distribution of ϕ produces a gradient in γ, the surface tension of the precursor liquid, and subsequently the driving force for droplet motion (Cira *et al.* 2015). Here, θ should be the static apparent contact angle measured under spatially uniform humidity conditions, rather than the dynamic angle during droplet motion.

Several empirical and theoretical relationships have been proposed to characterize the dependence of the apparent contact angle on the ambient humidity. Reported scalings range from $\theta \sim (\phi_{eq} - \phi)^{1/3}$ to $\theta \sim (\phi_{eq} - \phi)^{1/2}$, depending on whether evaporation-induced Marangoni flows are treated explicitly within a lubrication-theory framework (Karpitschka *et al.* 2017; Wu *et al.* 2021) or incorporated implicitly through effective interfacial relations (Cira *et al.* 2015). Careful experimental measurements typically yield effective exponents lying between these limiting values, reflecting the combined influence of thermodynamic and hydrodynamic effects near the contact line. Figure 3(*b*) shows our experimental data together with both scalings discussed. They capture the observed trends over the accessible humidity range, with minor quantitative differences that do not affect the droplet dynamics analysis.

Overall, these $\theta - \phi$ relationships supply surface tension variation combining evaporation, interfacial transport, compositional rearrangements and possible Marangoni-induced flows within the contact-line region, without the need to resolve the exact form of surface tension. They provide a basis for modelling the droplet dynamics addressed in this work.

3.2.4. *Inverse-square force and cubic kinematics*

Building on the humidity analysis and the experimental calibration of the humidity-dependent contact angle established above, we now quantify how the resulting surface tension heterogeneity generates a net driving force on a sessile droplet and governs its subsequent motion. As shown in (3.4), the capillary driving force acting on the sessile droplets originates from the circumferential variation of γ along the contact line. Projected onto the direction of motion, the force reads $F = \boldsymbol{F} \cdot \boldsymbol{e_x} = \int_0^{2\pi} \gamma \cos\varphi R \mathrm{d}\varphi$, where φ is the azimuthal angle, $\boldsymbol{e_x}$ is the unit vector in the x-direction, as illustrated schematically in figure 1(*b*). Under the quasistatic assumption, the humidity and the associated surface tension of the precursor film γ are assumed to remain slaved to the instantaneous droplet configuration. Accordingly, γ adjusts instantaneously to its local equilibrium value set by the humidity with $\gamma(\phi) = \gamma_d \cos\theta(\phi)$. Here θ parametrizes the macroscopic response of the contact line to humidity, rather than representing a dynamic contact angle during droplet motion. As mentioned above, contact angle is a function of humidity $\cos\theta = f(\phi)$. To simplify the analysis, $\cos\theta$ is expanded linearly,

$$f(\phi) \equiv \cos\theta = f'(\phi_\infty)(\phi - \phi_\infty) + f(\phi_\infty) = m\phi + b, \tag{3.11}$$

with $m = f'(\phi_\infty)$ and $b = -f'(\phi_\infty)\phi_\infty + f(\phi_\infty)$. Here

$$F = \int_0^{2\pi} \gamma_d \cos\theta \cos\varphi R \mathrm{d}\varphi = \gamma_d f'(\phi_\infty) \int_0^{2\pi} \phi R \cos\varphi \, \mathrm{d}\varphi. \tag{3.12}$$

Performing a local Taylor expansion of ϕ about the 'target' droplet centre gives

$$\int_0^{2\pi} \phi R \cos\varphi \, \mathrm{d}\varphi = \pi R^2 \frac{\partial \phi}{\partial d}, \tag{3.13}$$

where the zeroth-order contribution vanishes by angular symmetry. This expression shows that the driving force may be interpreted as the product of the wet area of the droplet and

https://doi.org/10.1017/jfm.2026.11903 Published online by Cambridge University Press

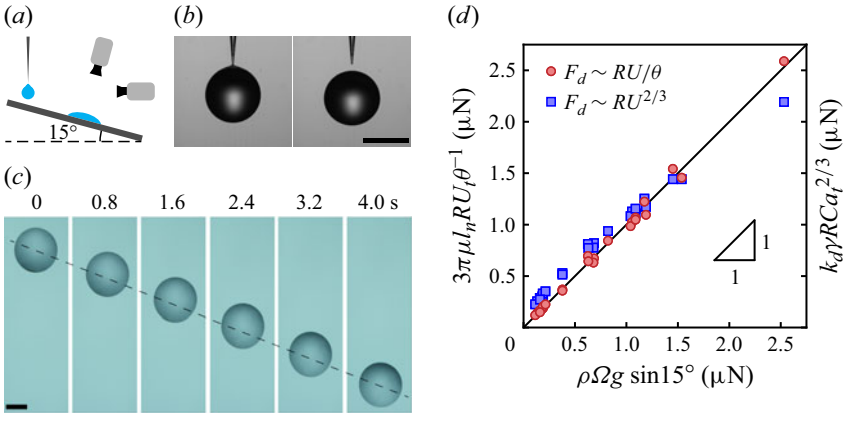


Figure 4. Inclined-plane sliding experiments used to assess the value of l_n by a moving droplet. (*a*) Schematic of a droplet on an inclined silicon wafer (15°). (*b*) Generation of a 10 wt % PG aqueous droplet of known volume Ω from a conical capillary tube (scale bar is 1 mm), ensuring reproducible gravitational force along the incline. (*c*) Droplet sliding on the inclined wafer at its terminal velocity (scale bar is 2 mm). (*d*) Comparison of the measured force–velocity relation with the linear scaling and the Cox–Voinov asymptotic form. The drag is evaluated against the component of gravity acting parallel to the substrate.

the vapour-induced surface-tension gradient evaluated along the direction of motion, with the latter given, to leading order in the humidity perturbation, by the directional derivative of the humidity field at the droplet centre. Therefore, the distribution of the humidity field contributes significantly to the functional form of the driving force. The resulting driving force reads

$$F = -\frac{\gamma_d m \lambda \pi R^3 (1-\phi_\infty)}{d^2}. \tag{3.14}$$

The higher-order terms contributing a relative correction can be neglected, which is discussed in the Supplementary material (§ II).

To close the dynamical problem, it is necessary to determine the coefficient appearing in (3.4). According to lubrication theory for droplets with small contact angles and low capillary number ($Ca \ll 1$), viscous dissipation is dominated by flow near the moving contact line, yielding a linear force–velocity relation $F_d = \xi\, \mu R U l_n/\theta$, where the dimensionless prefactor $\xi = 3\pi$ arises from the radial and circumferential integration of shear dissipation in the wedge-shaped lubrication flow (de Gennes 1985). Dedicated sliding experiments were then performed to quantify the logarithmic cutoff factor l_n associated with the motion of the same binary droplet, thereby closing the model. For comparison, we consider the Cox–Voinov asymptotic scaling (Voinov 1976; Cox 1986; de Gennes *et al.* 2003; Reyssat 2014), which predicts $F_d \sim \gamma\, R\, Ca^{2/3}$, reflecting the contribution of dynamic contact-angle effects to the viscous resistance (see the Supplementary material § IV).

As shown in figure 4(*d*), the measured force–velocity relation follows a linear scaling, with no distinct $Ca^{2/3}$ trend observed over the explored range. It may be attributed to Marangoni-induced contraction in binary droplets, as previously discussed in similar systems in Karpitschka *et al.* (2017) and Shiri *et al.* (2021).

Combining the driving force (3.14) with the measured drag F_d into (3.4) yields the droplet velocity

$$U = -k/(6d^2) = -k/[6(L+2R)^2], \tag{3.15}$$

https://doi.org/10.1017/jfm.2026.11903 Published online by Cambridge University Press

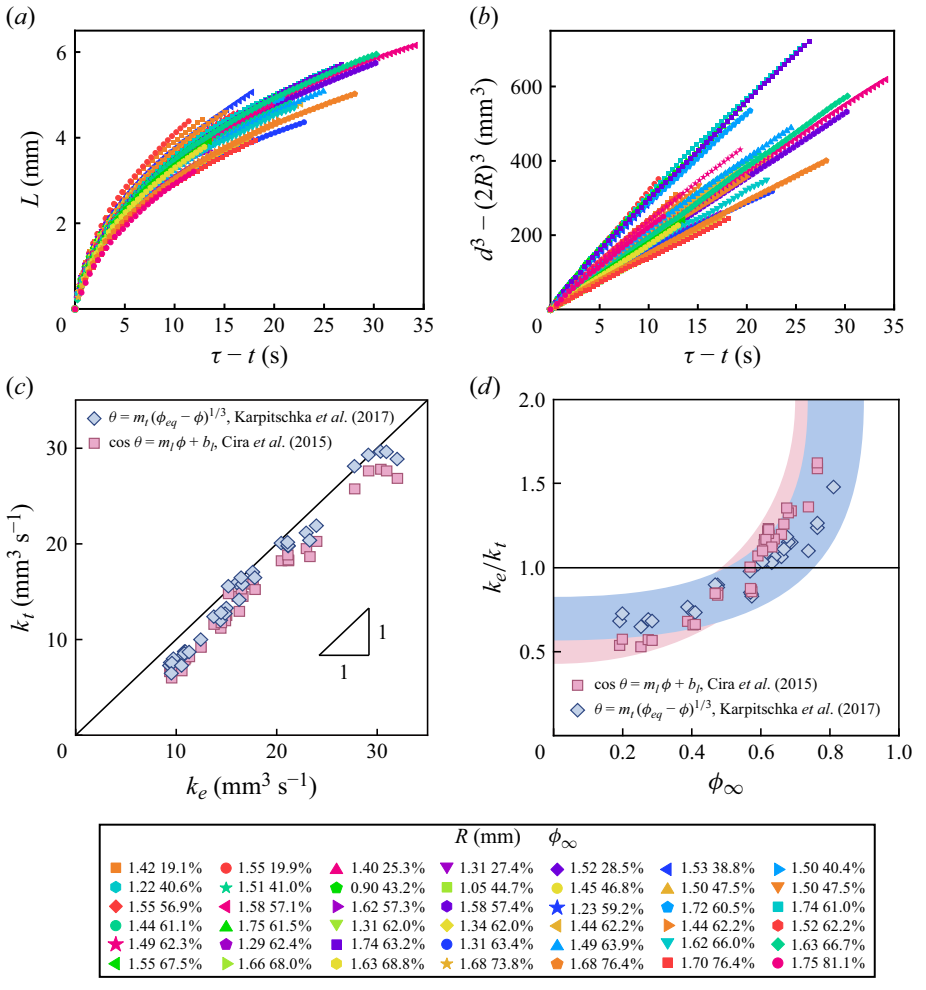


Figure 5. (*a*) Temporal evolution of the separation distance L as a function of $\tau - t$ for different droplet radii R and ambient relative humidities ϕ_∞. (*b*) The same data plotted in the rescaled representation collapse onto straight lines. The experiments span droplet radii in the range 0.8–1.8 mm and relative humidities from 19.9 % to 81.1 %. (*c*) Comparison between the prefactors k_t calculated theoretically from (3.15), and k_e measured experimentally from (*b*). Data are selected for $\phi_\infty \sim 60\,\%$. (*d*) The ratio of k_e/k_t versus environment humidity ϕ_∞. Fitting coefficients are $m_l = 0.036$ and $b_l = 0.96$, $m_t = 0.28$ and $\phi_{eq} = 0.95$.

where $k = 2\gamma_d m\lambda R^2\theta(1-\phi_\infty)/\mu l_n$. Integrating $2U = \mathrm{d}L/\mathrm{d}t$ yields a cubic kinematic scaling for the centre-to-centre distance $d = L + 2R$,

$$d^3 - (2R)^3 = k(\tau - t), \tag{3.16}$$

where τ denotes the time of contact.

Applying this transformation to the experimental data reveals a striking linear relation (figures 5*a* and 5*b*) that all curves collapse onto lines passing through the origin. This confirms that the observed droplet dynamics are consistent with the inverse-square force scaling of (3.14). These experiments covered droplet radii ranging from 0.8 to 1.8 mm and ϕ from 19.9 % to 81.1 %. Then, we compare the theoretical prefactor k_t computed from (3.15) with the experimentally extracted value k_e, as shown in figures 5(*c*) and 5(*d*).

https://doi.org/10.1017/jfm.2026.11903 Published online by Cambridge University Press

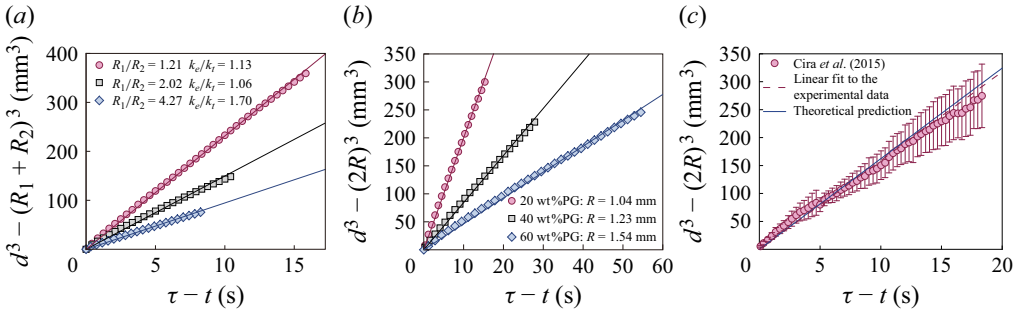


Figure 6. Comparison of the droplet kinematics under different experimental conditions. Here (*a*) 10 wt % PG droplet pairs with different initial radii. (*b*) Droplet pairs with identical PG concentration in each experiment, where the concentration is varied across different values. (*c*) Comparison between the theoretical prediction and experimental data reported by Cira *et al.* (2015), where the theoretical curves are evaluated using the parameters extracted from their measurements. The slope of the experimental fit, $k_e = 15.89$, is consistent with the theoretical value $k_t = 16.22$.

Good agreement is observed for $\phi_\infty \sim 60\,\%$ across both calibrations of $f(\phi)$. For more extreme experimental conditions with $\phi_\infty < 25\,\%$ or $> 75\,\%$, k_e/k_t calculated from both models deviates from 1, but still spreads mainly between 0.5 and 1.5. The deviation possibly originates from the use of $\theta = f(\phi_\infty)$ to predict the influence of local relative humidity on θ (figure 3*b*). A more precise model of $f(\phi)$ may be worth pursuing, nevertheless, it is shown from figure 5(*b*) that (3.16) holds for all tested experimental conditions with $\phi_\infty \in [19.1\,\%, 81.1\,\%]$, indicating the inverse-square nature of F is beyond reasonable doubt.

The effect of transient droplet deformation near the final stage of approach ($\tau - t \sim 0$) is shown to be negligible within the present parameter range (see the Supplementary material § V for details). Accordingly, the droplets may be treated as maintaining a fixed shape in the dynamical analysis. In addition, the maximum surface temperature difference induced by evaporative cooling is of order 10^{-3} K (Hu & Larson 2002). The associated thermally induced Marangoni force ($\sim 10^{-9}$ N) is at least two orders of magnitude smaller than the force arising from concentration-induced surface-tension gradients ($\sim 10^{-7}$ N). Evaporative thermal effects can therefore be safely neglected in the present dynamical analysis.

3.3. *Robustness of the inverse-square force*

We next examine the robustness of the driving force F within our PG-water droplet system, considering droplets of different sizes and concentrations. The first test is for two droplets of unequal size. Experimental results (figure 6*a*, also see Supplementary material (§ III and Supplementary movie 2)) show that

$$d^3 - (R_1 + R_2)^3 = k'(\tau - t), \tag{3.17}$$

where R_1, R_2 denote the spreading radii of the two droplets, respectively. The driving force of the 'target' droplet yields $F_{12} = -\lambda m \gamma_d \pi R_1 R_2^2 (1 - \phi_\infty)/d^2$, while the force acting on the 'source' droplet reads $F_{21} = -\lambda m \gamma_d \pi R_2 R_1^2 (1 - \phi_\infty)/d^2$. Here, the centre-to-centre distance is $d = L + R_1 + R_2$. It is evident that $F_{12} \neq F_{21}$ when $R_1 \neq R_2$, indicating they are not action and reaction forces. A complete derivation and accuracy analysis are provided in the Supplementary material (§ III). For moderate size ratios, the ratio k_e/k_t remains close to unity, while it increases to approximately 1.7 for large R_1/R_2.

https://doi.org/10.1017/jfm.2026.11903 Published online by Cambridge University Press

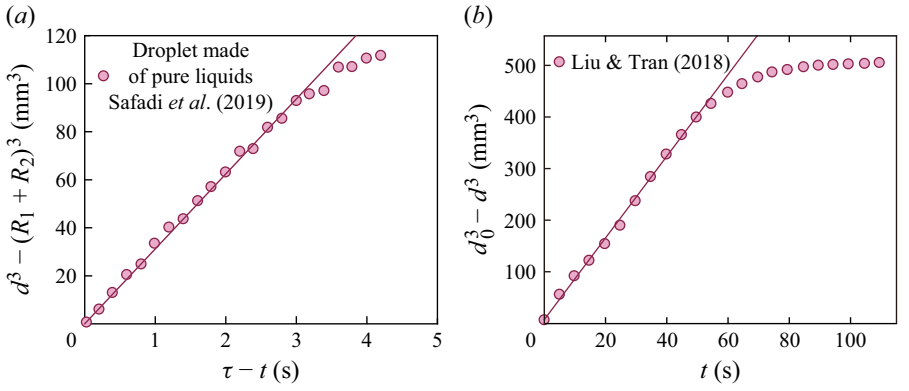


Figure 7. Kinematics of droplet motion driven by evaporative thermocapillary effects. Data fall into straight lines, consistent with theoretical predictions, demonstrating an inverse-square force between (*a*) droplets made of pure liquid (experimental data extracted from Sadafi *et al.* (2019)), and (*b*) two 80 wt % isopropyl alcohol aqueous droplets floating on a silicone oil pool (experimental data extracted from Liu & Tran (2018)). For (*b*), deviation occurs when thermally affected zones of two droplets overlap, which introduces additional hydrodynamic interactions and interferes with droplet motion.

Nevertheless, the inverse-square dependence of the driving force persists, indicating that the scaling is more robust than the detailed prefactor.

The same inverse-square interaction is observed when the droplet concentration is varied (figure 6*b*). Here, the concentration of two droplets is simultaneously selected as 20 wt %, 40 wt % and 60 wt %.

We further test the consistency of the theoretical model against experimental data reported by Cira *et al.* (2015). Using the parameters extracted from their measurements, the theoretical curve reproduces the observed behaviour. As shown in figure 6(*c*), the slope of the experimental fit, $k_e = 15.89$, is close to the theoretical value, $k_t = 16.22$, indicating that the inverse-square force scaling predicted by our theory is robust.

We extend the dynamical analysis to previously studied droplet systems, namely two pure *n*-Hexane droplets on a solid substrate (Sadafi *et al.* 2019) and floating binary droplets on a liquid free surface (Liu & Tran 2018). In both systems, interactions are mediated by undisturbed three-dimensional vapour or temperature fields. For the pure sessile droplets, motion is driven by evaporation-induced variations of the apparent contact angle and by thermal Marangoni stresses arising from substrate temperature gradients. For floating binary droplets, motion is driven by thermocapillary stresses induced by a temperature gradient across the droplet cap (Liu & Tran 2018). Both systems yield the same inverse-square interaction law, and in both cases the drag force scales linearly with droplet velocity. Accordingly, the droplet dynamics predict the same cubic scaling of distance with time, $d^3 \sim t$, as in our experiments (as derived from the droplet dynamics analyses in these studies; detailed derivations are provided in §§ VII and VIII of the Supplementary material). This prediction is confirmed by the kinematic data extracted from the previous studies, as shown in figure 7. To obtain a straight line through the origin, time t rather than $\tau - t$ in figure 7(*b*) is used to present the kinematic relationship. The reason is that the thermally affected zones of two droplets will overlap as distance d keeps decreasing, which in turn interferes with droplet motion, evidenced by data deviation from prediction for $t > 50$ s.

https://doi.org/10.1017/jfm.2026.11903 Published online by Cambridge University Press

4. Conclusion

Droplets are ubiquitous in natural phenomena and industrial applications, and precise control over their transport is a fundamental requirement for many physical and chemical processes. In this work, we have discovered an inverse-square force law between evaporating sessile droplets. When a target droplet is exposed to the spatially non-uniform vapour field generated by a neighbouring source droplet, the resulting asymmetric interfacial response near the contact line produces a non-zero net force. The inverse-distance decay of the vapour concentration around the source droplet is a key ingredient leading to the inverse-square dependence of this force on the centre-to-centre distance. The force law is supported by the cubic kinematic relation observed over ranges of droplet size, composition and ambient humidity.

The theory developed here combines continuum hydrodynamics with an effective capillary line-force representation of the localized interfacial stresses near the contact line. This representation distils the integrated effect of the strongly localized interfacial-stress variations and quantitatively captures the measured droplet dynamics, without requiring full resolution of the microscopic Marangoni flow, compositional transport and contact-line motion. The conditions under which this simplified capillary treatment becomes quantitatively equivalent to a full hydrodynamic treatment remain to be fully established. Such equivalence is expected to depend primarily on the localization of the interfacial stresses, the vapour-induced contact-line response and the dominant hydrodynamic dissipation mechanism.

The present results suggest that an inverse-square force can arise when a diffusion-controlled scalar field couples to a localized asymmetric interfacial-stress response and the resulting droplet motion remains quasistatic. Its broader applicability is further supported by our analysis of previously published kinematic data for pure-liquid sessile droplets and thermocapillary floating droplets. The cubic kinematic relation also provides a practical diagnostic for identifying an inverse-square driving force from droplet trajectories. This diagnostic is experimentally accessible and does not require full resolution of the microscopic flow field. In multidroplet systems, however, the vapour field is not necessarily a simple linear superposition, especially when neighbouring fields overlap and the local relative humidity approaches saturation. Confined geometries may further modify the scalar-field decay and hence the force. These effects define natural directions for future work.

Supplementary materials and movies. Supplementary materials and movies are available at https://doi.org/10.1017/jfm.2026.11903.

Funding. This study was supported by the National Natural Science Foundation of China (12388101, 11972339, 11932019).

Declaration of interests. The authors report no conflict of interest.

References

BANGHAM, D.H. & SAWERIS, Z. 1938 The behaviour of liquid drops and adsorbed films at cleavage surfaces of mica. *Trans. Faraday Soc.* **34**, 554–570.

BENUSIGLIO, A., CIRA, N., LAI, A.W. & PRAKASH, M. 2017 Two-component self-contracted droplets: long-range attraction and confinement effects. arXiv:1711.06404.

CHAO, Y., RAMÍREZ-SOTO, O., BAHR, C. & KARPITSCHKA, S. 2022 How liquid–liquid phase separation induces active spreading. *Proc. Natl Acad. Sci. USA* **119** (30), e2203510119.

CIRA, N.J., BENUSIGLIO, A. & PRAKASH, M. 2015 Vapour-mediated sensing and motility in two-component droplets. *Nature* **519** (7544), 446–450.

COX, R.G. 1986 The dynamics of the spreading of liquids on a solid surface. Part 1. Viscous flow. *J. Fluid Mech.* **168**, 169–194.

https://doi.org/10.1017/jfm.2026.11903 Published online by Cambridge University Press

DEEGAN, R.D., BAKAJIN, O., DUPONT, T.F., HUBER, G., NAGEL, S.R. & WITTEN, T.A. 1997 Capillary flow as the cause of ring stains from dried liquid drops. *Nature* **389** (6653), 827–829.
DEEGAN, R.D., BAKAJIN, O., DUPONT, T.F., HUBER, G., NAGEL, S.R. & WITTEN, T.A. 2000 Contact line deposits in an evaporating drop. *Phys. Rev. E* **62** (1), 756.
DEKKER, P.J., ROCHA, D., LOHSE, D. & DIDDENS, C. 2026 Internal flow and concentration in neighbouring evaporating binary droplets and rivulets. *J. Fluid Mech.* **1032**, A33.
DIDDENS, C. 2017 Detailed finite element method modeling of evaporating multi-component droplets. *J. Comput. Phys.* **340**, 670–687.
DIDDENS, C., KUERTEN, J.G.M., VAN DER GELD, C.W.M. & WIJSHOFF, H.M.A. 2017*a* Modeling the evaporation of sessile multi-component droplets. *J. Colloid Interface Sci.* **487**, 426–436.
DIDDENS, C., TAN, H., LV, P., VERSLUIS, M., KUERTEN, J.G.M., ZHANG, X. & LOHSE, D. 2017*b* Evaporating pure, binary and ternary droplets: thermal effects and axial symmetry breaking. *J. Fluid Mech.* **823**, 470–497.
GELDERBLOM, H., DIDDENS, C. & MARIN, A. 2022 Evaporation-driven liquid flow in sessile droplets. *Soft Matt.* **18** (45), 8535–8553.
DE GENNES, P.-G. 1985 Wetting: statics and dynamics. *Rev. Mod. Phys.* **57** (3), 827.
DE GENNES, P.-G., BROCHARD-WYART, F. & QUÉRÉ, D. 2003 *Capillarity and Wetting Phenomena: Drops, Bubbles, Pearls, Waves*. Springer.
HACK, M.A., KWIECINSKI, W., RAMÍREZ-SOTO, O., SEGERS, T., KARPITSCHKA, S., KOOIJ, E.S. & SNOEIJER, J.H. 2021 Wetting of two-component drops: Marangoni contraction versus autophobing. *Langmuir* **37** (12), 3605–3611.
HAPPEL, J. & BRENNER, H. 2012 *Low Reynolds Number Hydrodynamics: With Special Applications to Particulate Media*, vol. 1. Springer Science & Business Media.
HU, H. & LARSON, R.G. 2002 Evaporation of a sessile droplet on a substrate. *J. Phys. Chem. B* **106** (6), 1334–1344.
KARPITSCHKA, S., LIEBIG, F. & RIEGLER, H. 2017 Marangoni contraction of evaporating sessile droplets of binary mixtures. *Langmuir* **33** (19), 4682–4687.
LIU, D. & TRAN, T. 2018 Vapor-induced attraction of floating droplets. *J. Phys. Chem. Lett.* **9** (16), 4771–4775.
LOHSE, D. & ZHANG, X. 2020 Physicochemical hydrodynamics of droplets out of equilibrium. *Nat. Rev. Phys.* **2** (8), 426–443.
MALINOWSKI, R., PARKIN, I.P. & VOLPE, G. 2020 Nonmonotonic contactless manipulation of binary droplets via sensing of localized vapor sources on pristine substrates. *Sci. Adv.* **6** (40), eaba3636.
MAN, X. & DOI, M. 2017 Vapor-induced motion of liquid droplets on an inert substrate. *Phys. Rev. Lett.* **119** (4), 044502.
MASOUD, H., HOWELL, P.D. & STONE, H.A. 2021 Evaporation of multiple droplets. *J. Fluid Mech.* **927**, R4.
MASOUD, H. & STONE, H.A. 2014 A reciprocal theorem for Marangoni propulsion. *J. Fluid Mech.* **741**, R4.
MASOUD, H. & STONE, H.A. 2019 The reciprocal theorem in fluid dynamics and transport phenomena. *J. Fluid Mech.* **879**, P1.
PICKNETT, R.G. & BEXON, R. 1977 The evaporation of sessile or pendant drops in still air. *J. Colloid Interface Sci.* **61** (2), 336–350.
RAMÍREZ-SOTO, O. & KARPITSCHKA, S. 2022 Taylor dispersion in thin liquid films of volatile mixtures: a quantitative model for Marangoni contraction. *Phys. Rev. Fluids* **7** (2), L022001.
RAOULT, F.-M. 1887 Loi générale des tensions de vapeur des dissolvants. *C. R. Hebd. Séances Acad. Sci.* **104**, 1430–1433.
REYSSAT, E. 2014 Drops and bubbles in wedges. *J. Fluid Mech.* **748**, 641–662.
RYU, J., DIDDENS, C., LOHSE, D. & KIM, H. 2025 Vapour-driven solutal Marangoni flow transition across the vapour–liquid equilibrium at the droplet contact line. *J. Fluid Mech.* **1019**, A3.
SADAFI, H., DEHAECK, S., BLACKNIKOV, A. & COLINET, P. 2019 Vapor-mediated versus substrate-mediated interactions between volatile droplets. *Langmuir* **35** (21), 7060–7065.
SAXENA, P. & HILDEMANN, L.M. 1997 Water absorption by organics: survey of laboratory evidence and evaluation of UNIFAC for estimating water activity. *Environ. Sci. Technol.* **31** (11), 3318–3324.
SHIRI, S., SINHA, S., BAUMGARTNER, D.A. & CIRA, N.J. 2021 Thermal marangoni flow impacts the shape of single component volatile droplets on thin, completely wetting substrates. *Phys. Rev. Lett.* **127** (2), 024502.
SNOEIJER, J.H. & ANDREOTTI, B. 2013 Moving contact lines: scales, regimes, and dynamical transitions. *Annu. Rev. Fluid Mech.* **45** (1), 269–292.
STULL, D.R. 2002 Vapor pressure of pure substances. Organic and inorganic compounds. *Ind. Engng Chem.* **39** (4), 517–550.

https://doi.org/10.1017/jfm.2026.11903 Published online by Cambridge University Press

VOINOV, O.V. 1976 Hydrodynamics of wetting. *Fluid Dyn.* **11** (5), 714–721.

WAGNER, W. & PRUSS, A. 2002 The IAPWS formulation 1995 for the thermodynamic properties of ordinary water substance for general and scientific use. *J. Phys. Chem. Ref. Data* **31** (2), 387–535.

WANG, Z., KARAPETSAS, G., VALLURI, P., SEFIANE, K., WILLIAMS, A. & TAKATA, Y. 2021 Dynamics of hygroscopic aqueous solution droplets undergoing evaporation or vapour absorption. *J. Fluid Mech.* **912**, A2.

WILLIAMS, A.G.L., KARAPETSAS, G., MAMALIS, D., SEFIANE, K., MATAR, O.K. & VALLURI, P. 2021 Spreading and retraction dynamics of sessile evaporating droplets comprising volatile binary mixtures. *J. Fluid Mech.* **907**, A22.

WILSON, S.K. & D'AMBROSIO, H.-M. 2023 Evaporation of sessile droplets. *Annu. Rev. Fluid Mech.* **55**, 481–509.

WU, M., DOI, M. & MAN, X. 2021 The contact angle of an evaporating droplet of a binary solution on a super wetting surface. *Soft Matt.* **17** (34), 7932–7939.

ZHAO, H., OREJON, D., SEFIANE, K. & SHANAHAN, M.E.R. 2025 Long-range vapor-mediated interactions between adjacent droplets. *Langmuir* **41** (6), 3986–3994.

https://doi.org/10.1017/jfm.2026.11903 Published online by Cambridge University Press